Rapid Analysis of Trinitite with Nuclear Forensic Applications for Post-Detonation Material Analyses

Nicholas Sharp [a*], William F. McDonough[a, b*], Brian W. Ticknor[c], Richard D. Ash[b], Philip M. Piccoli[b], Dana T. Borg[b]

[a]Department of Chemistry & Biochemistry
University of Maryland
College Park, MD 20742
USA

[b]Department of Geology
University of Maryland
College Park, MD 20742
USA

[c]Chemical Sciences Division
Oak Ridge National Laboratory
1 Bethel Valley Road, MS 6415
Oak Ridge TN 37830
USA

*Corresponding authors:
Nicholas Sharp
Department of Chemistry & Biochemistry
University of Maryland
College Park, MD 20742
USA
Tel: (301)405-1830
Fax: (301)405-3597
nsharp@umd.edu

William F. McDonough
Department of Geology
University of Maryland
College Park, MD 20742
USA
Tel: (301) 405-5561
Fax: (301) 405-3597
mcdonoug@umd.edu

Keywords: Trinitite * Nuclear Forensics * Laser-ablation and solution inductively coupled mass spectrometry * Nd and Gd isotopic ratios

Abstract

Analysis of post-nuclear detonation materials provides information on the type of device and its origin. Compositional analysis of trinitite glass, fused silicate material produced from the above ground plasma during the detonation of the Trinity nuclear bomb, reveals gross scale chemical and isotopic heterogeneities indicative of limited convective re-homogenization during accumulation into a melt pool at ground zero. Regions rich in weapons grade Pu have also been identified on the surface of the trinitite sample. The absolute and relative abundances of the lanthanoids in the glass are comparable to that of average upper crust composition, whereas the isotopic abundances of key lanthanoids are distinctly non-normal. The trinitite glass has a non-normal Nd isotope composition, with deviations of -1.66 ± 0.48 ε (differences in parts in 10^4) in $^{142}Nd/^{144}Nd$, +2.24 ± 0.32 ε in $^{145}Nd/^{144}Nd$, and +1.00 ± 0.66 ε in $^{148}Nd/^{144}Nd$ (all errors cited at 2σ) relative to reference materials: BHVO-2 and Nd-Ames metal. Greater isotopic deviations are found in Gd, with enrichments of +4.28 ± 0.72 ε in $^{155}Gd/^{160}Gd$, +4.19 ± 0.56 ε in $^{156}Gd/^{160}Gd$, and +3.59 ± 0.37 ε in $^{158}Gd/^{160}Gd$ compared to BHVO-2. The isotopic deviations are consistent with a ^{239}Pu based fission device with additional ^{235}U fission contribution and a thermal neutron fluence between 0.97 and 1.4 x 10^{15} neutrons/cm^2.

Introduction

Today, a well-documented chemical and isotopic database is needed to assign origin and provenance to materials from a nuclear event. Characterizing the fissile material and composition of an unknown device are central efforts of nuclear forensics which can be challenging in the case of an urban event, given the myriad of debris types possible from the local environment. In the case of a nuclear device, non-natural isotopic fingerprints have the potential to provide insights into the history, source, and origin of interdicted materials. It is critical to observe and understand the effects of a fission event on less-complicated material before embarking on analyzing complex urban debris. Analyses of trinitite, fused silica-glass from the Trinity test event, presents nuclear forensic investigators with ideal post-detonation material where the composition of the nuclear device and source material are well-known, enabling validation of testing methods designed to determine a device's original makeup. In this study, we present chemical and isotopic data on trinitite and compare our results with Trinity's known characteristics.

In the early hours of 16 July 1945 the atomic age began with the Trinity nuclear bomb detonation at the White Sands Proving Ground, New Mexico. The bomb, a ^{239}Pu implosion device, produced a fireball of 10^4 K and a debris cloud that reached a height of 11 km within minutes, and eventually as high as 21 km [1]. The debris cloud, consisting of material from the detonation tower, the bomb itself, and adjacent desert sand, precipitated onto the desert floor and cooled rapidly, yielding a glassy surface, trinitite, that surrounded the explosion site.

The four varieties of trinitite include: green glass trinitite, pancake trinitite, red trinitite, and bead trinitite. All types originate from arkosic sand and are composed of quartz, microcline, albite, muscovite, actinolite, and calcite [1]. The green glass variety (analyzed in this study)

86 consists of glass with no observable unaltered original sand material. This sample was likely
87 produced from the combination of proximal sand near ground zero melting into a glass and
88 falling material from the debris cloud [2]. However, due to remediation of the test site, the exact
89 location relative to ground-zero for this trinitite sample is unknown.
90 Trinitite contains fissile materials, neutron activated materials, and pieces of the detonation
91 tower and the bomb itself, such as the uranium tamper and lead casing [2-4]. Recently uranium
92 and lead isotopic signatures of the bomb have been investigated [5, 6]. Here we report on the
93 chemical and isotopic composition of trinitite, both spatially resolved laser ablation and solution
94 analyses, using inductively coupled plasma mass spectrometry. During detonation, fission
95 products of both light and heavy isotopes (e.g., 80-105 amu and 130-160 amu, respectively) are
96 produced. The tail of the heavy isotope product distribution includes the middle members of the
97 lanthanoids. The relative isotopic abundances of lanthanoids produced via fission differ from
98 those occurring naturally. The mixing of fission lanthanoids with natural material produces
99 measurable enrichments and depletions in isotopic abundances when compared to natural
100 material. The resultant altered isotopic abundances can be used to identify the device's fissile
101 material, given a successful deconvolution of the fissile and natural isotopic compositions.
102 In this study the concentration of major element oxides and lanthanoids were determined
103 using a combination of electron probe micro-analysis (EPMA) and laser-ablation inductively-
104 coupled mass spectrometry (LA-ICP-MS). The isotopic composition of Gd and Nd were
105 determined by sample dissolution followed by chromatographic separation of the elements of
106 interest using multi-collector inductively coupled plasma mass spectrometry (MC-ICP-MS). The
107 utility of rapid analysis of a post-detonation material via EPMA and LA-ICP-MS provides an

initial qualitative screening that readily identifies specific targets for more thorough analyses, in this case using MC-ICP-MS for high-precision isotopic ratio determinations.

Experimental methods

The trinitite sample studied is entirely glass and contains little to no original sand. The green glass has a smooth top which corresponds to the surface facing the atmosphere during deposition. Deeper into the sample are vesicles with increasing frequency with greater depth. Samples are highly heterogeneous in composition with vesicles accounting for approximately 33% of the total trinitite volume [7]. A ~1 g piece was broken off of the bulk pool glass and subsequently split into two fractions by hand. Both were mounted in epoxy: one piece was mounted with the smooth surface exposed; the other piece was mounted perpendicular to the smooth surface (cross section; Fig 1**)**.

Electron microprobe

The JXA-8900 SuperProbe was used to determine major element concentrations via wavelength dispersive spectrometry (WDS). The analyses were carried out with a 10-20 μm spot size, accelerating voltage of 15 kV, and a 20 nA cup current. Data was recalculated using a ZAF algorithm using orthoclase (K_2O, Al_2O_3, SiO_2), rhodonite (MnO), and kakanui hornblende (CaO, MgO, FeO, TiO_2) as primary standards with Yellowstone rhyolite as a secondary standard. Backscattered electron (BSE) images were also acquired.

Sample digestion and chromatography

For Nd and Gd isotope analysis a 0.1 g piece of trinitite underwent an acid digestion procedure consisting of a mixture of concentrated HNO_3 and HF in addition to 100 µL of $HClO_4$ in a sealed 15 mL Teflon beaker. Two 0.05 g BHVO-2 SRMs underwent the same procedure in separate beakers. An analytical blank was also prepared and treated with the same chemistry procedure and resulted in Nd and Gd blank concentrations of 6 pg. Teflon distilled acid was used for sample digesting, chromatography, and sample analysis.

Sample digestion was performed on a hotplate set to 180°C for 72 hours. Subsequently the beakers were opened and the solutions were dried to a hard residual cake; 6 M HCl was added to each beaker, and they were then resealed and heated for an additional 24 hours. Following this heating, the beakers were opened and allowed to dry again, and the 6M HCl step was repeated. After the 3rd drying step 2 mL of quartz distilled 2.5 M HCl was added to the samples.

Lanthanoids were separated from the bulk matrix with a 12cm x 2cm Dowex AG50W x8 400 mesh cation exchange column in H^+ form. The 2 mL solution of 2.5 M HCl was added to the column and 50 mL of 2.5 M HCl wash was added and followed by 45 mL of 4.5 M HNO_3, with the last 35 mL collected as the REE cut. The REE cut was then dried down and reconstituted in 0.5 mL of 0.15 M α-hydroxyisobutyric acid (α-HIBA) buffered at pH 4.7 using NH_4OH.

Individual lanthanoids were separated using a 30 cm x 0.5 cm column filled with Dowex AG50W x8 400 mesh cation exchange resin treated with concentrated NH_4OH to convert the resin from H^+ to the NH_4^+ form. The 0.5 mL sample solution was loaded and followed by a

series of elution steps with α-HIBA isolating the Nd and Gd cuts. The Nd and Gd cuts were then dried down and then dissolved with 2 mL of 0.8 M HNO_3. Isotope analysis samples were prepared by taking 300 μL of the cut solution diluted with 1.2 mL of 0.8 M HNO_3.

LA-ICP-MS and MC-ICP-MS

The laser ablation analyses were conducted on a single collector, sector field, Element 2 (Thermo-Finnigan, Bremen, Germany) ICP-MS coupled to a 213 nm wavelength laser ablation system (UP213, New Wave Research) with operating conditions detailed in Table 1. Optimization of the instrument included tuning the ion lenses and ICP-MS torch position to maximize the signals at masses 43, 139 and 178 while maintaining $^{238}U^{16}O/^{238}U \leq 0.2\%$. Individual analysis included a 30s background acquisition followed by 30s spot analysis.

An external standard of NIST610 was analyzed in duplicate at the beginning and end of each data acquisition of ~16 spots analyses of unknowns. Differences in beam diameter were due to higher concentrations of lanthanoids in NIST610 compared to trinitite. The absolute concentration of Ca obtained from EMPA analyses functioned as an internal calibrant for data processing with LAMTRACE [8]. For laser ablation sites not constrained by EPMA determined Ca concentration, the laser ablation data was corrected by normalizing the ablation yields of unconstrained Ca sites to the ablation yields of EPMA constrained Ca sites. Plutonium concentrations are based on the assumption that Pu ablates at approximately the same efficiency as U. This correction allowed for the determination of a concentration/signal ratio for U at each site and to apply that factor to the Pu signal to determine a first-order approximation of Pu concentration.

Isotope analyses for Nd and Gd were conducted at the University of Maryland Geology (UMD) department and the Savannah River National Laboratory (SRNL) using Nu Plasma HR MC-ICP-MS (Nu Instruments, Wrexham, UK) with operating parameters listed in Table 2. The instrument at UMD was coupled to an Aridus I (Cetac Technologies, Omaha, NE) desolvating nebulizer while a DSN-100 desolvating nebulizer (Nu Instruments) was coupled to the mass spectrometer at SRNL. Measurement parameters were identical at each location with 5 blocks of 20 10 second integration points with a mandatory 30 second background determination at the beginning of each block.

Isobaric interferences for Nd consisted of Ce and Sm at masses: 142, 144, 148, and 150. During sample acquisition, ^{140}Ce remained stable at ≤1.3mV while ^{147}Sm remained at ≤1x10^{-2} mV; the contribution from Sm isobars was negligible, whereas interference from Ce required a correction to ^{142}Nd using ^{142}Ce/^{140}Ce = 0.1256[9].

Instrument induced mass fractionation for Nd was corrected on-line by normalizing to ^{146}Nd/^{144}Nd = 0.7219. Normalizing using 0.7219 is not ideal due to fission production of ^{146}Nd and ^{144}Nd, however, the comparable fission isotopic ratio of 0.6667 permits us to make comparisons using the original 0.7219 value for mass fractionation correction. In the case of Gd a concentration standard was mass fractionation corrected using ^{156}Gd/^{160}Gd = 0.9361 and the mass bias factor from this correction was used to correct the BHVO-2 and trinitite data. Due to low signals of ^{152}Gd and ^{154}Gd (80mV and 8mV, respectively) those isotopes are not reported.

Results

A vertical cross section through a ~1 cm thick piece of trinitite glass reveals chemical and physical heterogeneities. The sample top surface (i.e., that facing the atmosphere) and subjacent region contains silicate glass populated with quartz grains that show signs of incipient melting. A vertical gradient in the amount and size of vesicles with increasing sample depth into the puddle glass is observed (Fig. 2). The lower portion of the cross section (3.0-5.5mm below the surface) contains a higher abundance of partially-melted quartz grains. The incipiently melted material present on the bottom of the sample most likely remained on the desert floor and was not incorporated into the debris cloud, resulting in less overall melting and more vesicles. The quartz-rich zones appear more pronounced lower in the cross-section.

Major oxide compositions determined using EPMA are listed in Table 3. There is marked bulk compositional heterogeneity of the cross section of trinitite glass (Fig. 2+3) with CaO and FeO concentration increasing with depth and K_2O and Al_2O_3 concentrations decreasing with depth. We observed positive correlation of FeO vs CaO and K_2O vs Al_2O_3 and negative correlation of FeO vs Al_2O_3 and CaO vs K_2O (Fig. 3). Lanthanoid concentrations obtained via LA-ICP-MS (Table 4) on average show that the trinitite glass is comparable to the average upper crust composition (Fig. 4) [10], however, some domains show marked depletion, possibly reflecting lithological variations in the available desert floor and are likely due to high calcite and quartz contributions.

Analyses at selected sites show ^{238}U and ^{239}Pu (Table 4) concentrations vary by an order of magnitude and are not correlated with other elemental concentrations in the sample. In general, all sites analyzed exhibited a $^{240}Pu/^{239}Pu$ ratio of ≤ 0.03, which is indicative of weapons

grade Pu [12], a strong marker for the fissile material used in the device. In-situ laser ablation also identified isotopic anamolies in Gd isotopic ratios (Fig. 5) which provided strong evidence that more rigorous analyses of the trinitite sample were warranted and would likely yield detailed information about the fission device.

The Nd isotopic composition for trinitite is distinctive from both the BHVO-2 and Nd-Ames metal solution (Table 5) reference materials, and shows deviations in $^{142}Nd/^{144}Nd$, $^{145}Nd/^{144}Nd$, and $^{148}Nd/^{144}Nd$ which are -1.66 ε, +2.24 ε, and +1.00 ε respectively, with ε being deviations in parts in 10^4. Likewise, the Gd isotopic composition of trinitite (Table 3) also differs from natural materials in $^{155}Gd/^{160}Gd$, $^{156}Gd/^{160}Gd$, and $^{158}Gd/^{160}Gd$ with enrichments of 4.28 ε, 4.19 ε, and 3.59 ε respectively.

Discussion

Vertical, textural, and chemical gradations in the trinitite glass are consistent with rapidly quenched melt material that was not sufficiently molten long enough for thermal convection to efficiently mix and homogenize the melt pool. The top 1 mm is suggestive of the source material primarily consisting of potassium feldspar, $KAlSi_3O_8$, which agrees with one of the possible glass forms identified in previous studies [13]. The smooth texture of the sample's surface alone is not sufficient to determine how the sample was produced. The top-most material could either have been original desert floor which was heated to melting from the thermal radiation of the blast, or it could consist of molten droplets raining from the sky and pooling over the desert floor [2,13]. The primarily potassium feldspar composition of the analyzed region does not imply that the top material is solely potassium feldspar, instead, it shows that an original crystal of

potassium feldspar was melted to such a degree that it is not visually observable from its surroundings.

The observable increase in vesicle frequency with cross-sectional depth could be due to degassing of water from the beneath the desert floor. The topmost layer of trinitite likely consists of material that rained out from the debris cloud, which was degassed and vesicle free. The initial blast and early deposited material on the desert floor heated pre-existing local water to evaporation. The deposition of airborne material incorporated desert floor sediments and acted as an insulator while the top-most layer quenched to a glass. Degasing likely occurred deeper in the soil with the vapors escaping upward to the quenched surface, becoming trapped and creating vesicles of increasing size with depth in the sample. An alternative explanation by Belloni *et al*. [2] proposed that immediately following the detonation the sand around ground zero is heated to its boiling point. Roughly 2 seconds after the explosion, molten droplets begin to rain down on the boiling sand, forming the top-most portion of trinitite. Trinitite is then instantly quenched by cool air being sucked toward ground zero.

Nd and Gd isotopic composition

Deviations in the isotopic ratios of Nd and Gd in trinitite are dominated by two nuclear processes: neutron absorption and fission product generation. Neutron absorption reactions, specifically thermal (~0.025 eV) neutron capture, will decrease the abundance of an isotope that has a large neutron capture cross-section, with an accompanying increase in the capture products, while isotopes with comparatively low cross sections would have a reduced probability for neutron capture, thus remaining largely unaffected. Thermal neutrons are specifically mentioned

here as fast neutrons (greater than 0.5 MeV) have a lower probability of being captured by nuclei due to their higher energy and must undergo several kinetic collisions with other nuclei before becoming thermalized and able to participate in capture reactions. Fast neutrons can also participate in nuclear reactions outside of neutron capture, however, our calculations specifically require thermal neutrons and, therefore, we are constrained to reporting the thermal neutron fluence of Trinity and not the total neutron fluence.

None of the Nd isotopes are major neutron absorbers, thus neutron absorption reactions do not play a prominent role in any Nd isotopic deviations found in trinitite. However, two Gd isotopes, ^{155}Gd and ^{157}Gd, have large capture cross-sections for thermal neutrons, $6x10^4$ b and $2.5x10^5$ b respectively. Their resulting capture products, ^{156}Gd and ^{158}Gd, exhibit very small capture cross-sections for thermal neutrons, 1.8 b and 2.2 b respectively, which are too low to experience significant depletions, resulting in enrichments in ^{156}Gd and ^{158}Gd which can be directly correlated with depletions in ^{155}Gd and ^{157}Gd.

Fission also changes the Nd and Gd isotopic ratios due to decay of neutron-rich fission products. Trinity's ^{239}Pu fast fission does not immediately produce significant stable Nd and Gd isotopes (highest yield being 0.1% and .001% respectively [14]), however, after subsequent beta decays, stable isotopes are produced with yields found in Table 6. Fission produced isotope yields alone are not sufficient to predict deviations in isotopic ratios. To predict isotopic ratio deviations the difference between the isotopic composition of fissioned material and natural material must be taken into account. If a fission event produces isotopes in similar abundances to natural material at most a small deviation will be observed. For example, ^{146}Nd/^{144}Nd in natural material is assumed to be 0.7219, however, in ^{239}Pu fission the ratio is 0.6669, resulting in a maximum deviation of -762 ε. However, if the fission event produces isotopes that are

greatly different than natural material a large deviation will be observed. For example, $^{155}Gd/^{160}Gd$ in most natural material is assumed to be 0.6768, however, the ratio produced in ^{239}Pu fission is 13.13, resulting in a maximum deviation of +184,000 ε.

Maximum deviations can only be observed when the fission event was of such magnitude that the element's natural mass has been overwhelmed with fission produced material and has a pure fission composition. Thus, both the yield and isotopic composition of the fissioned material must be considered when predicting deviations in isotopic composition of fallout material. Lower concentrations of lanthanoids in natural material are more sensitive to both fission isotope generation and neutron capture due to the lower number of atoms available to dilute the fissionogenic signature. Therefore, we would expect to observe the most pronounced altered isotopic abundances in elements that are both low abundance in nature and produced in high yields via fission; both criteria that are met by Nd and Gd.

There is a noticeable difference in time domains of neutron lifetimes (on the order of tens of seconds [15]) and time necessary for beta decay of fission products to reach stable lanthanoid isotopes (hours-Table 6). This difference in time enables a simplifying assumption that neutron capture only occurred on naturally occurring material, essentially no fission product lanthanoids were available or participated in neutron capture. For example, ^{157}Gd has an independent fission yield of $3x10^{-5}$% whereas the majority of mass 157 isotopes are produced as ^{157}Sm ($t_{1/2}$ = 8.03 minutes) with a yield of ~0.1%. It takes approximately 160 minutes for all ^{157}Sm to beta decay to ^{157}Gd, by which time neutrons are no longer available for capture. Immediately produced lanthanoid fission product nuclei can also be assumed to not participate in neutron capture reactions due to their neutron heavy structure and relatively low capture cross sections in comparison to the naturally stable lanthanoids. The lanthanoids produced through fission with

high immediate yields are so neutron rich that they all have short half-lives, on the order of mintues, and undergo β^- decay. With the neutron pulse being on the order of seconds and the half-lives on the order of minutes it can be assumed that none of the lanthanoids immediately produced via fission absorb any neutrons. Therefore, the only lanthanoids able to absorb neutrons were already present in the natural source material.

Having neutron absorption occur prior to β-decay of neutron-rich fission products enables an iterative modeling process to determine the total neutron fluence the trinitite sample experienced. The isotopic composition of Gd and Nd can also be used to determine whether ^{235}U or ^{239}Pu was the fissile material, based on their distinctive fission product isotopic composition. The iterative process begins by determining the total number of atoms for each isotope initially present and then determining the effect of unknown neutron fluence on the isotopic composition using the following equation:

$$N_{x+1}^{c} = N_{x+1}^{\circ} + \left(N_{x}^{\circ} * \sigma_{c}^{x} - N_{x+1}^{\circ} * \sigma_{c}^{x+1}\right) * \Phi \quad (1)$$

where N_x° represents the original atoms of isotope x, N_{x+1}^c the resulting atoms of isotope x+1, σ_c^x is the neutron capture cross section of isotope x in cm^2, and the total neutron fluence is Φ.

Fission products are introduced according to their cumulative yields using the general equation:

$$N_{x}^{f} = N_{x}^{c} + \rho_{x}^{cum} * Fission\ Events \quad (2)$$

where N_x^f and N_x^c representspost-fission and post-neutron capture atoms, respectively, and ρ_x^{cum} represents the cumulative fission yield of isotope x. The number of fission events is increased until the modeled isotopic ratios are of similar magnitude as the measured ratios from trinitite. Both equation steps are repeated in an iterative process until a best fit line has been reached.

As previously mentioned, a low capture cross section for thermal neutrons results in Nd isotopes having low sensitivity to neutron fluence, and therefore are not ideal for determining the level of neutron fluence produced by the Trinity detonation. With the larger neutron capture cross-sections in Gd, the neutron fluence can be back-calculated based on Gd isotopic ratios. The neutron fluence can be calculated in two ways: the iterative process previously detailed or by using equation 3:

$$\Phi_N = \frac{\left[\left(\frac{^{158}Gd}{^{157}Gd}\right)_t - \left(\frac{^{158}Gd}{^{157}Gd}\right)_n\right]}{\sigma_{157}\left[1+\left(\frac{^{158}Gd}{^{157}Gd}\right)_n\right]+\left[0.25\sigma_{155}\left(\frac{^{158}Gd}{^{157}Gd}\right)_n * \left(\frac{^{155}Gd}{^{156}Gd}\right)_n\right]} \quad (3)$$

Equation 3 was derived by Eugster et al. [16], with Φ_N representing thermal neutron fluence in n/cm^2, the subscripts t and n represent trinitite and natural, and σ_x is the thermal neutron capture cross section for their respective isotopes.

The iterative process gives a fluence value of 1.4±0.2x10^{15} n/cm^2 (all errors cited at 2σ), which is on the lower end of the values predicted by Parekh et al. [17], while calculations based on Gd ratios results in a fluence of 9.468±0.002x10^{14} n/cm^2. The differing uncertainties are a product of calculating the total mass of Gd experimentally measured ion current from the faraday cup for the iterative process. This signal has a greater uncertainty due to fluctuations in the ion beam compared to the uncertainty of the isotope ratio pairs, which constrain the ratio calculation method. The discrepancy between these two fluence values could be due to the ratio method not accounting for fission product interference, which would reduce the impact of neutron capture on ^{155}Gd/^{156}Gd and ^{157}Gd/^{158}Gd given the greater production of ^{155}Gd and ^{157}Gd compared to ^{156}Gd and ^{158}Gd respectively.

Trinity's fissile material can be determined by looking at the isotopic ratios of Gd (Fig. 6). The isotopic ratios, which would be obtained from fissioning either ^{235}U or ^{239}Pu, are

similar with regards to $^{156}Gd/^{160}Gd$, $^{157}Gd/^{160}Gd$, and $^{158}Gd/^{160}Gd$. However, a noticeable depletion in $^{155}Gd/^{160}Gd$ is observed relative to modeled predictions. Based on scaling ^{239}Pu and ^{235}U fissionogenic isotopic ratios to trinitite, ^{235}U fission would have resulted in +12 ε enrichment in $^{155}Gd/^{160}Gd$ while ^{239}Pu would have resulted in +5.8 ε. Both possible fissile materials show an enrichment above what is actually observed in this trinitite sample for ^{155}Gd, however, the lower limit for ^{239}Pu is within 3 standard deviations of the measured value whereas ^{235}U is ~22 standard deviations. The closer agreement observed for ^{239}Pu is a strong indicator that ^{239}Pu was the fissile material as opposed to ^{235}U.

The isotopic ratios of Nd show clear signs of fissionogenic contribution due to enrichments in $^{145}Nd/^{144}Nd$ and $^{148}Nd/^{144}Nd$ and depletions in $^{142}Nd/^{144}Nd$ (Fig. 7). As previously mentioned, Nd isotopic deviations occur solely due to yield of fission isotopes which peaks at ^{144}Nd (Table 6). The depletion in $^{142}Nd/^{144}Nd$ is due to the lack of production of ^{142}Nd compared to ^{144}Nd. The presence of stable ^{142}Ce along the decay path of mass 142 fission products results in no additional production of ^{142}Nd with the exception of the small likelihood of ^{142}Pr production (10^{-6}%) or direct production of ^{142}Nd (10^{-10}%). The scaling fit for the initial fissile material shows strong agreement for ^{239}Pu based on $^{142}Nd/^{144}Nd$, $^{145}Nd/^{144}Nd$, and $^{146}Nd/^{144}Nd$. However, $^{148}Nd/^{144}Nd$ fits between the ^{239}Pu and ^{235}U fission curves along with $^{150}Nd/^{144}Nd$, which is not distinguishable from natural material. The greater uncertainty in ^{148}Nd and ^{150}Nd isotopic ratios is due to their lower abundances and large mass differences compared to the mass fractionation correction ratio, and could explain the deviation of trinitite values from the ^{239}Pu fission curve.

Conversely, $^{150}Nd/^{144}Nd$ does not show any signs of enrichment, which was expected given that ^{239}Pu fission production would yield an isotopic ratio of 0.269±5, greater than the

measured natural isotopic ratio of 0.236353±9 (Table 5) for Nd-Ames metal. Assuming ^{239}Pu fission, trinitite should exhibit enrichment in ^{150}Nd/^{144}Nd compared to natural. Possible explanations for this discrepancy include loss of fission produced ^{150}Nd or a greater production of ^{144}Nd than expected. However, due to the agreement with the other isotopic ratios with the ^{239}Pu model the ^{144}Nd excess is unlikely and the preferential loss of ^{150}Nd compared to the other isotopes is also unlikely to occur. Neutron capture on ^{150}Nd isotopes is unlikely due to the 1 b neutron capture cross section of ^{150}Nd.

Another possible explanation is production of Nd through ^{235}U fast neutron fission, which would give ^{150}Nd/^{144}Nd and ^{148}Nd/^{144}Nd isotopic ratios of 0.182±6 and 0.140±3 respectively [14], lower than the ratios produced from fast fission of ^{239}Pu which are 0.269±5 and 0.449±9 respectively. The trinitite ^{148}Nd/^{144}Nd and ^{150}Nd/^{144}Nd ratios plot between the ^{239}Pu and ^{235}U fast fission predictions. Recent studies have also shown that other isotopic systems plot between both ^{239}Pu and ^{235}U fission [18]. The presence of notable isotopic alterations caused by ^{235}U fission suggests that ^{235}U fission contributed significantly to the overall fission events from Trinity, in addition to the ^{239}Pu which was the primary fissile material. Our model isn't able to assign a quantified value to the ^{235}U fission contribution, but our results arein agreement with modeled predictions made by Semkow et al. 2007 [19] and noted discrepancies in predicted ^{155}Eu and ^{137}Cs ratios by Bellucci et al. [18]. Evidence for ^{235}U fission is not apparent in Gd isotopes, due to the difference in yields of Gd through ^{235}U and ^{239}Pu fission. Fission of ^{239}Pu produces approximately 10x the amount of Gd per fission event compared to ^{235}U (Table 6), therefore, the ^{239}Pu events obfuscated any possible ^{235}U contribution.

The ability to determine the fissile material used in a nuclear weapon from the isotopic composition of rare earth elements in post-detonation material provides investigators with a

method that is more resistant to artificial emulation with fissile material or common highly radioactive fission products. Results from this method can be used in tandem with other indicators of a fission device to verify or bring into question a previous hypothesis concerning the fissile material used in the device. Focusing specifically on Trinity, the combination of the presence of ^{239}Pu and the non-normal isotopic compositions of Nd and Gd provides compelling evidence that Trinity was a primarily ^{239}Pu based fission device with additional fission contribution from ^{235}U.

Conclusion

The trinitite sample analyzed in this study has significant variability with depth in terms of major element compositions and vesicle abundance. Signs of the fission event are apparent in the isotopic composition of Nd and Gd with clear enrichments and deviations in normally invariable ratios. Comparison of trinitite Nd isotopic composition with ^{239}Pu and ^{235}U fission predictions yielded evidence of fission of not only ^{239}Pu, which the device was intended to fission, but also significant fission of ^{235}U. Detecting the contribution of unexpected fissile material in Trinity highlights the level of detail that can be obtained using careful sampling and analysis of post-detonation material. Taking advantage of rapid analysis times achievable with EPMA and LA-ICP-MS, a first pass analysis of any intercepted or post-detonation nuclear material can be performed quickly while also identifying suitable samples for more in-depth analyses.

Acknowledgments

We would like to thank the Smithsonian National Museum of Natural History for the trinitite sample, A. Fahey for discussion over trinitite properties and sample analysis techniques, and Savannah River National Laboratory for the use of their mass spectrometer. NS adds a special thanks to Dr. Mignerey for her assistance in understanding neutron and fission interactions. Funding was provided by the Plasma Lab at the University of Maryland, the Department of Geology, and the University of Maryland.

References

1. Eby N, Hermes R, Charnley N, Smoliga JA (2010) Trinitite—the atomic rock. *GeolToday* 26(5):180-185
2. Belloni F, Himbert J, Marzocchi O, Romanello V (2011) Investigating incorporation and distribution of radionuclides in trinitite. *J of Environ Radioact* 102(9):852-862
3. Fahey AJ, Zeissler CJ, Newbury DE, Davis J, Lindstrom RM (2010) Postdetonation nuclear debris for attribution. *Proc Natl Acad of Sci USA* 107(47):20207-20212
4. Bellucci J, Simonetti A (2012)Nuclear forensics: Searching for nuclear device debris in trinitite-hosted inclusions. *J Radioanl Nucl Chem 293(1):313-319*
5. Bellucci JJ, Simonetti A, Wallace C, Koeman EC, Burns PC (2013) Isotopic fingerprinting of the world's first nuclear device using post-detonation materials. *Anal Chem* 85(8):4195-4198
6. Bellucci JJ, Simonetti A, Wallace C, Koeman EC, Burns PC (2013) Lead isotopic composition of trinitite melt glass: Evidence for the presence of Canadian industrial lead in the first atomic weapon test. *Anal Chem* 85(15):7588-7593
7. Hermes RE, Strickfaden WB (2005) A new look at trinitite. Nucl Weapons J (2):2-7.
8. Jackson S (2008) LAMTRACE data reduction software for LA-ICP-MS. *Laser Ablation ICP-MS Earth Sci Curr Pract and Outst Issues*, Mineral Assoc of Can, Short Course Ser 40:305-307
9. Chang T-L, Qian Q-Y, Zhao M-T, Wang J, Lang Q-Y (1995) The absolute isotopic composition of cerium. *Int J Mass Spectrom and Ion Process* 142(1–2):125-131
10. Rudnick RL, Gao S (2003) Composition of the Continental Crust. Treatise Geochem 3:1-64
11. Barth MG, McDonough WF, Rudnick RL (2000) Tracking the budget of Nb and Ta in the continental crust. *Chem Geol* 165(3-4):197-213
12. Moody K, Hutcheon I, Grant P (2005) Nuclear Forensic Analysis. Boca Raton, FL
13. Ross CS (1948) Optical properties of glass from Alamogordo, New Mexico. *Am Mineral* 33:360-362
14. Chadwick MB, Herman M, Obložinský P, Dunn ME, Danon Y, Kahler AC, Smith DL, Pritychenko B, Arbanas G, Arcilla R, Brewer R, Brown DA, Capote R, Carlson AD, Cho YS, Derrien H, Guber K, Hale GM, Hoblit S, Holloway S, Johnson TD, Kawano T, Kiedrowski BC, Kim H, Kunieda S, Larson NM, Leal L, Lestone JP, Little RC, McCutchan EA, MacFarlane RE, MacInnes M, Mattoon CM, McKnight RD, Mughabghab SF, Nobre GPA, Palmiotti G, Palumbo A, Pigni MT, Pronyaev VG, Sayer RO, Sonzogni AA, Summers NC, Talou P, Thompson IJ, Trkov A, Vogt RL, van der Marck SC, Wallner A, White MC, Wiarda D, Young PG (2011) ENDF/B-VII.1 Nuclear data for science and technology: Cross sections, covariances, fission product yields and decay data. *Nucl Data Sheets* 112(12):2887-2996
15. Bainbridge, KT (1976) Trinity. (*No. LA-6300-H*). Los Alamos Scientific Lab., NM (USA).
16. Eugster O, Tera F, Burnett DS, Wasserburg G (1970) Isotopic composition of gadolinium and neutron-capture effects in some meteorites. *J Geophys Res* 75(14):2753-2768
17. Parekh PP, Semkow TM, Torres MA, Haines DK, Cooper JM, Rosenberg PM, Kitto ME (2006) Raioactivity in Trinitite six decades later. *J. Environ. Radioact.* 85: 103-120

18. Bellucci JJ, Wallace C, Koeman EC, Simonetti A, Burns PC, Kieser J, Port E, Walczak T (2013) Distribution and behavior of some radionuclides associated with the Trinity nuclear test. *J Radioanal Nucl Chem* 295(3):2049-205719. Semkow TM, Parekh PP, Haines DK (2006) Modeling the effects of the Trinity test. *Appl. Model Comput. Nucl. Sci.* 142-159

Figure Legends

Fig. 1 BSE image of the two pieces of trinitite mounted in epoxy. The piece on the top is the smooth surface of a piece of trinitite while the bottom image is the cross sectional piece in Figure 1. The boxes are LA-ICP-MS sites, the circles are EPMA sites, and the triangles are sites that were analyzed with both methods

Fig. 2 Cross section BSE image of trinitite showing an increase in size and number of vesicles with depth and EPMA sites marked E1-7. Darker shades of gray represent partially melted quartz grains. Uncertainty in the concentration measurements are on the order of ± 1% (2σ)

Fig. 3 Correlation of major elements in trinitite cross section. Uncertainties here are ±1% (2σ) and are smaller than the data points

Fig. 4 Comparison of lanthanoid concentrations obtained with LA-ICP-MS on trinitite. Values are normalized to upper crust values from Rudnick and Gao [10]. Loess (grey region), a glacial dust which is a naturally produced sample of the average upper continental crust [11], are compared to trinitite. Average trinitite values (black squares) represent average from n=7 analyses, with L1 and L9 plotted separately. Uncertainties shown are 2σ. The Gd values for L1 and L9 are below detection and are therefore empty markers

Fig. 5 Isotopic composition of Gd analyzed with LA-ICP-MS. Mixing line represents line from ^{239}Pu fission production to natural composition. Icelandic basalt (BIR) was used as a secondary standard during analyses

Fig. 6 Graph of ε (10^4) deviation in trinitite for Gd isotopes normalized to ^{160}Gd. Uncertainty reported as 2σ. Trinitite and BHVO-2 were corrected for mass fractionation via sample-standard bracketing with a concentration standard corrected to ^{156}Gd/^{160}Gd = 0.9361. Shaded regions refer to 2σ uncertainty with ^{235}U model uncertainty comparable to ^{239}Pu

Fig. 7 Graph of ε (10^4) deviation in trinitite for Nd isotopes, normalized to ^{144}Nd, from an average value of Nd-Ames metal and BHVO-2. Uncertainty reported as 2σ. BHVO-2 ratios are shown compared to the averaged natural value to show instrumental precision. Interferences in BHVO-2 and trinitite were observed at ^{140}Ce signal <1 mV and ^{147}Sm<10^{-3} mV. Results for ^{142}Nd are corrected for ^{142}Ce interference. All isotopic ratios are corrected to ^{146}Nd/^{144}Nd = 0.7219. Shaded regions refer to 2σ uncertainty with ^{235}U model uncertainty comparable to ^{239}Pu

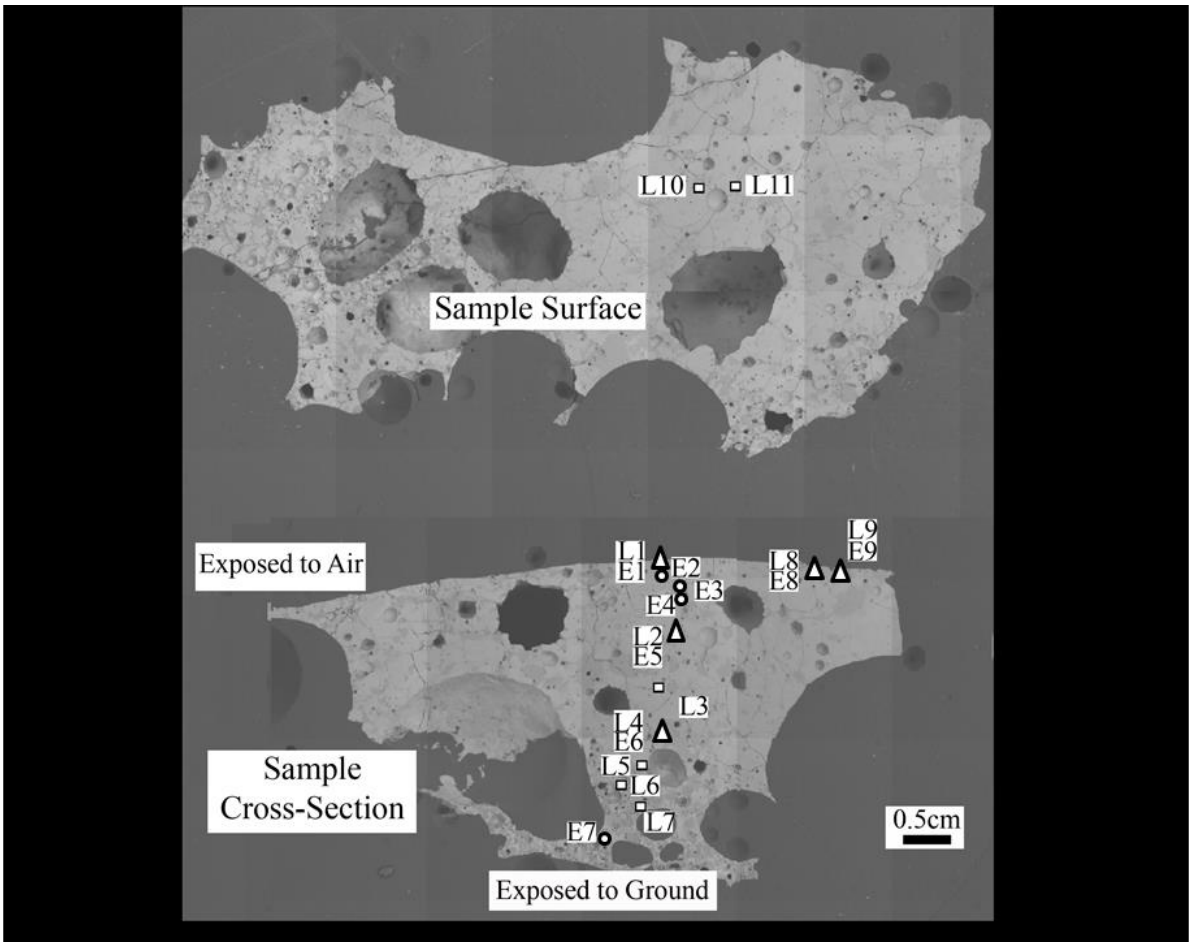

Fig. 1 BSE image of the two pieces of trinitite mounted in epoxy. The piece on the top is the smooth surface of a piece of trinitite while the bottom image is the cross sectional piece in Fig. 1. The boxes are LA-ICP-MS sites, the circles are EPMA sites, and the triangles are sites that were analyzed with both methods.

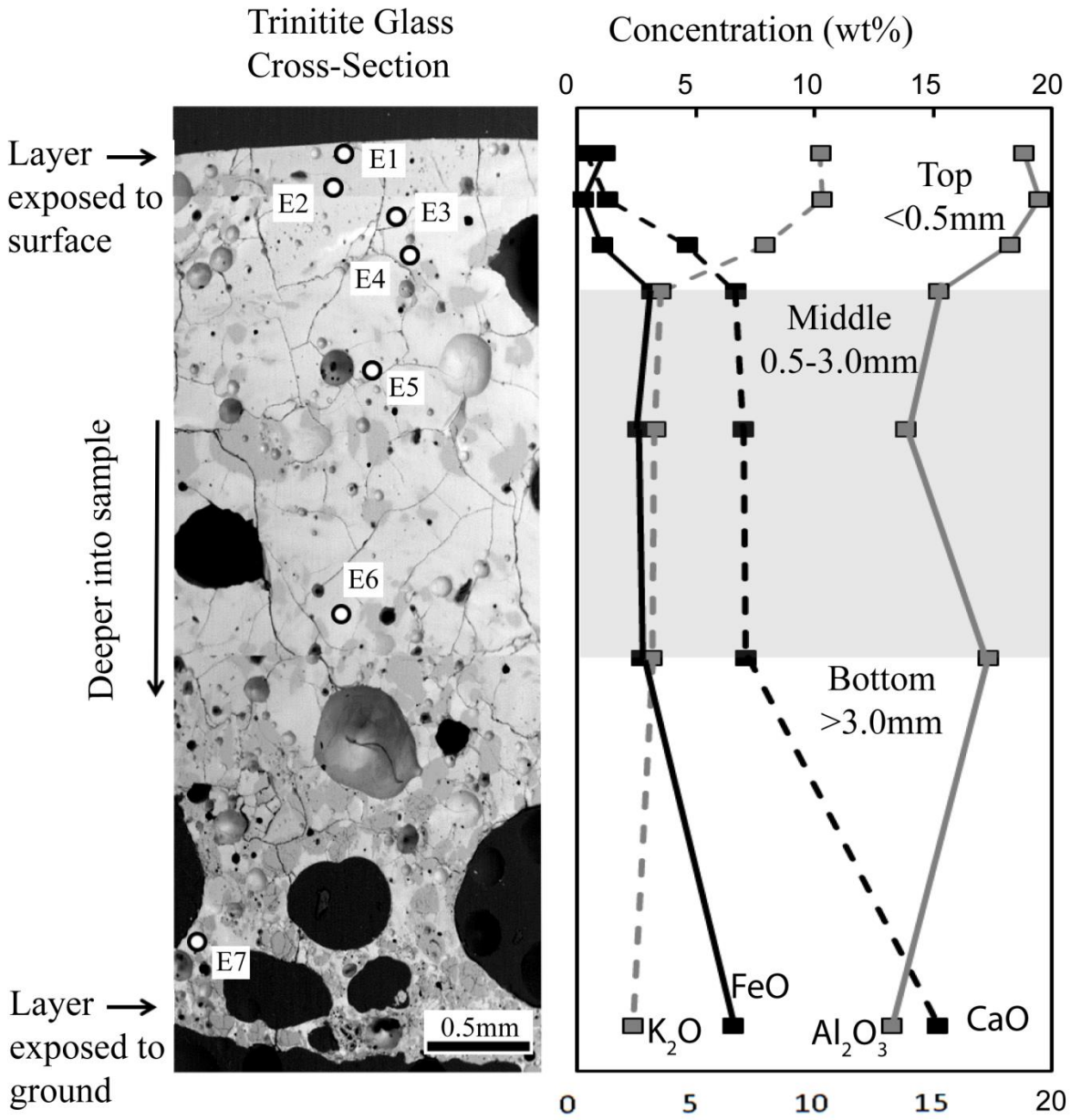

Fig. 2 Cross section BSE image of trinitite showing an increase in size and number of vesicles with depth and EPMA sites marked E1-7. Darker shades of gray represent partially melted quartz grains. Uncertainty in the concentration measurements are on the order of ± 1% (2σ).

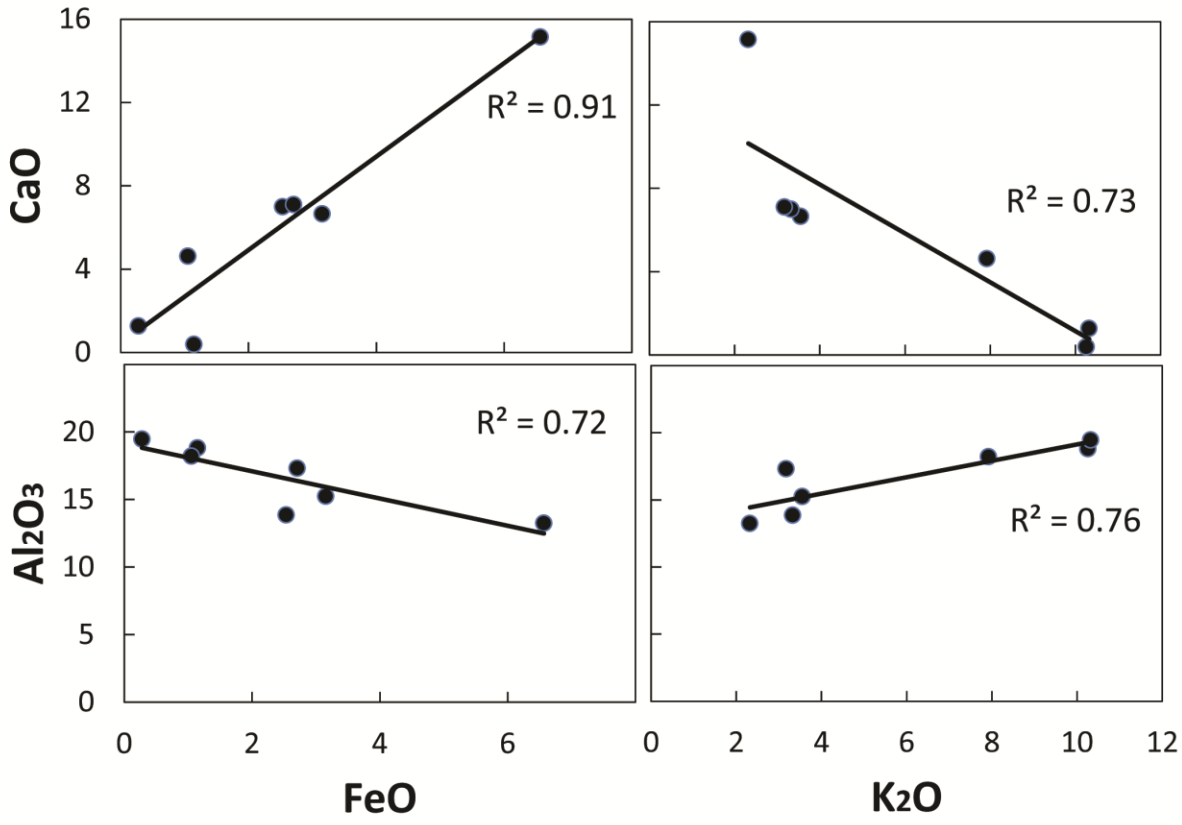

Fig. 3 Correlation of major elements in trinitite cross section. Uncertainties are ±1% (2σ) and are smaller than the data points.

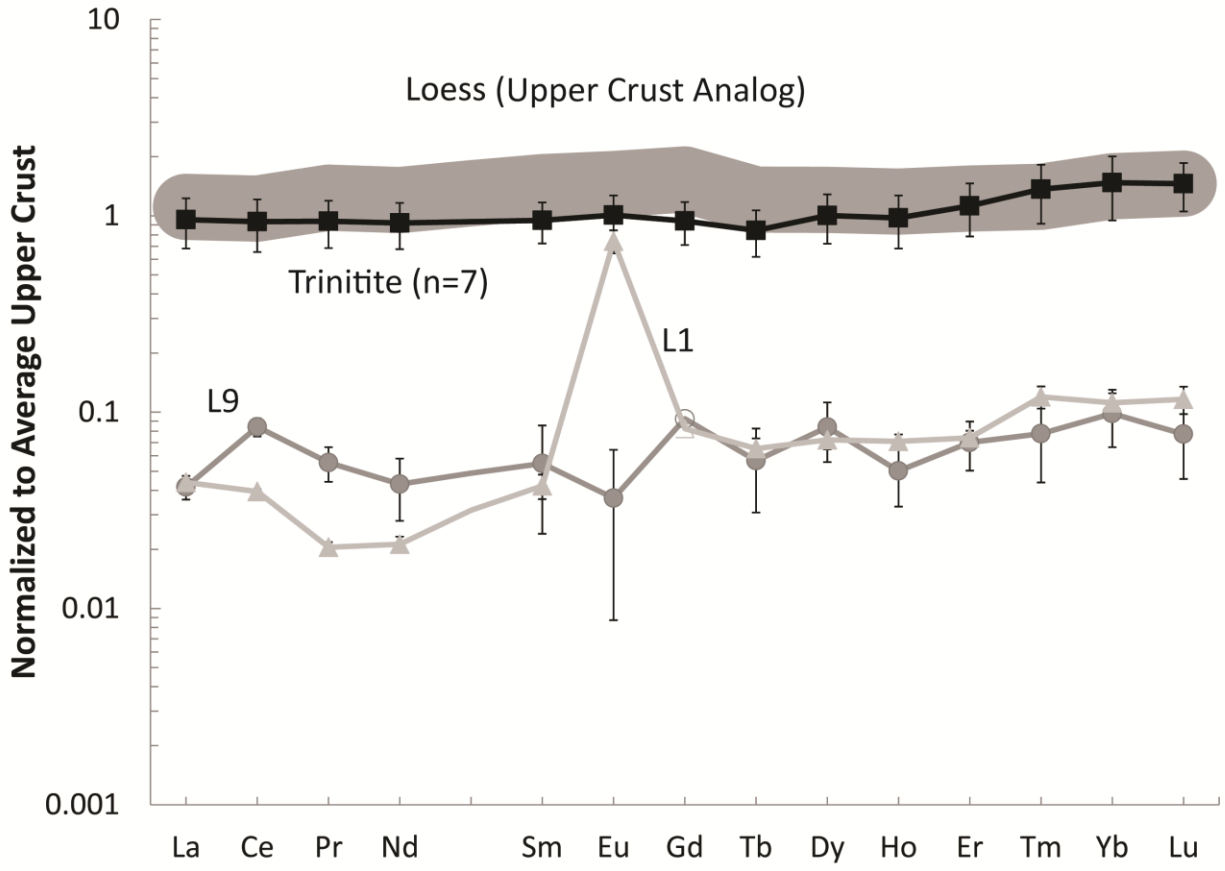

552
553
554 **Fig. 4** Comparison of lanthanoid concentrations obtained with LA-ICP-MS on trinitite. Values
555 are normalized to upper crust values from Rudnick and Gao [10]. Loess (grey region), a glacial
556 dust which is a naturally produced sample of the average upper continental crust [11], are
557 compared to trinitite. Average trinitite values (black squares) represent average from n=7
558 analyses, with L1 and L9 plotted separately. Uncertainties shown are 2σ. The Gd values for L1
559 and L9 are below detection and are therefore empty markers.
560

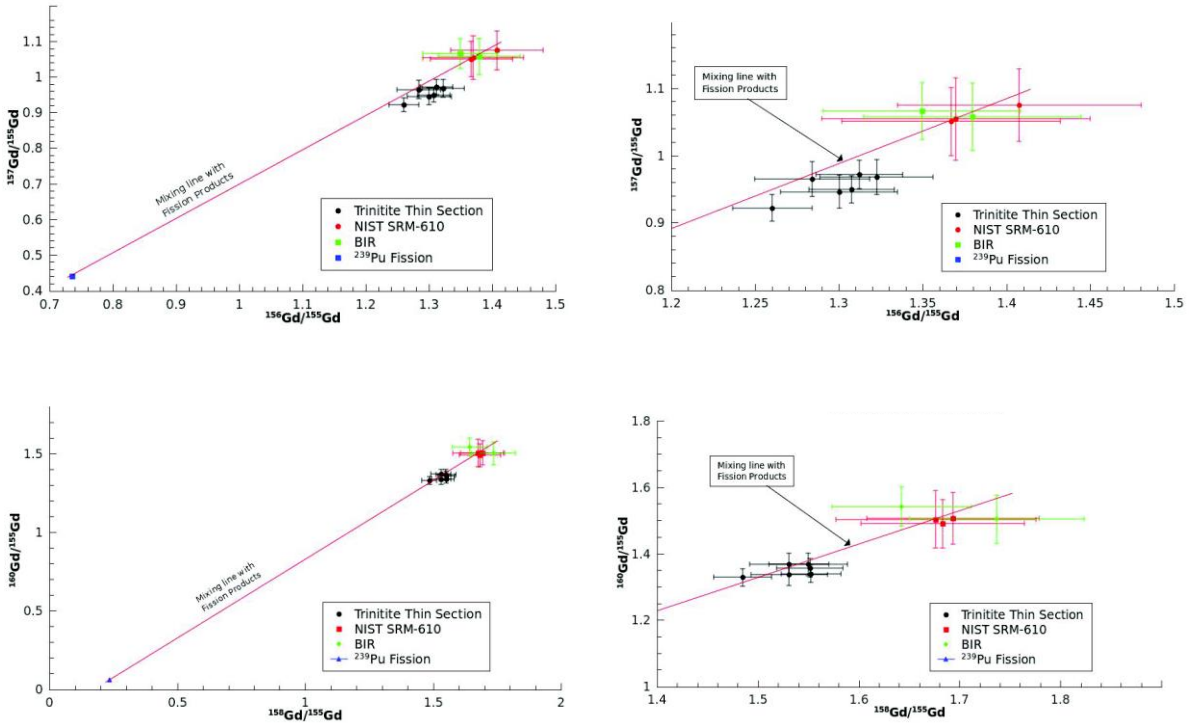

Fig. 5 Isotopic composition of Gd analyzed with LA-ICP-MS. Mixing line represents line from ^{239}Pu fission production to natural composition. Icelandic basalt (BIR) was used as a secondary standard during analyses.

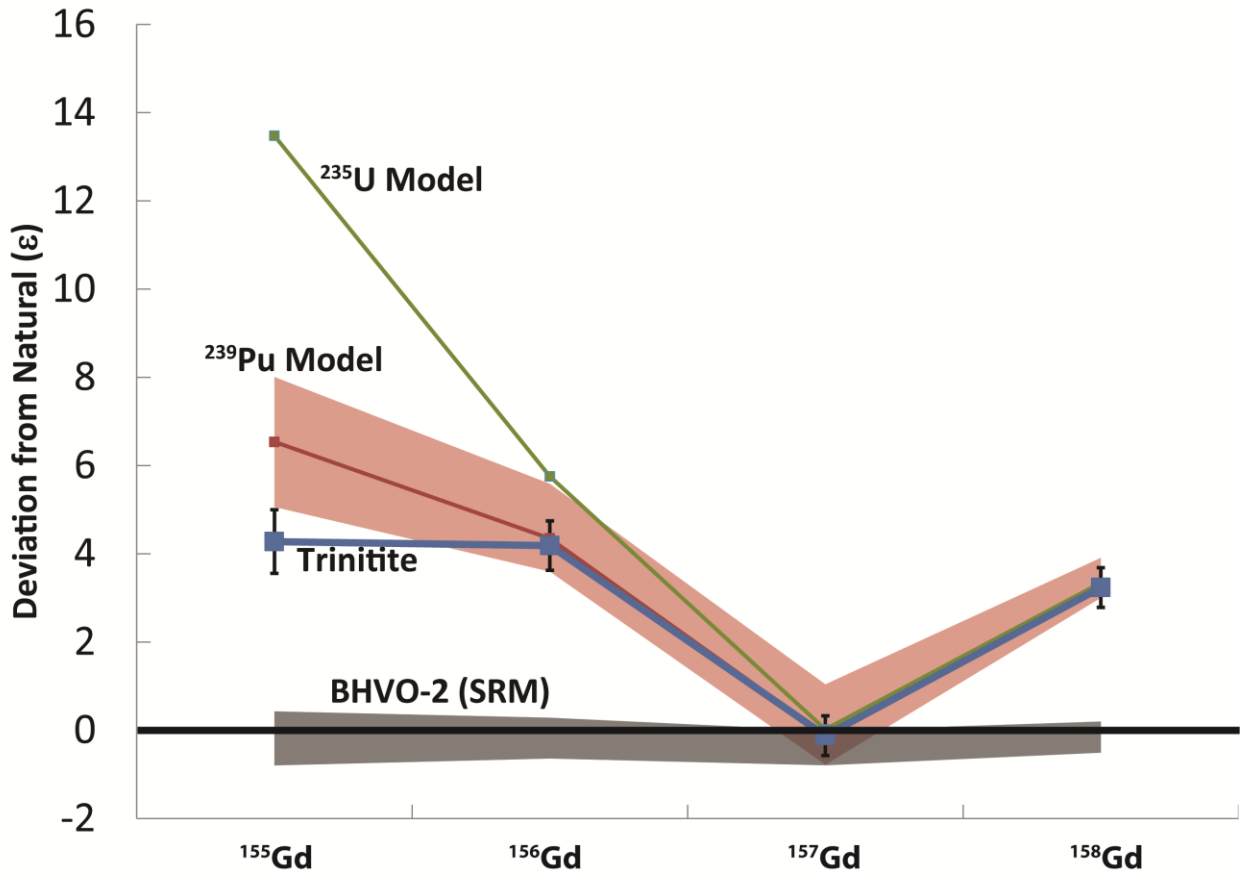

Fig. 6 Graph of ε (10^4) deviation in trinitite for Gd isotopes normalized to ^{160}Gd. Uncertainty reported as 2σ. Trinitite and BHVO-2 were corrected for mass fractionation via sample-standard bracketing with a concentration standard corrected to ^{156}Gd/^{160}Gd = 0.9361. Shaded regions refer to 2σ uncertainty with ^{235}U model uncertainty comparable to ^{239}Pu.

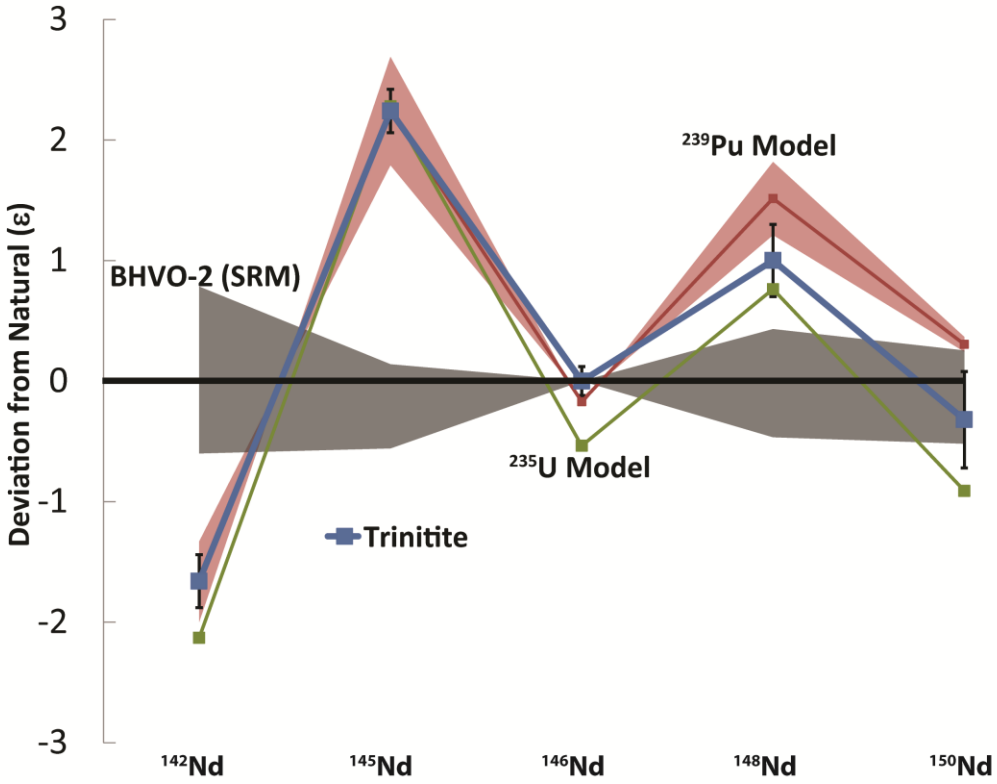

Fig. 7 Graph of ε (10^4) deviation in trinitite for Nd isotopes, normalized to ^{144}Nd, from an average value of Nd-Ames metal and BHVO-2. Uncertainty reported as 2σ. BHVO-2 ratios are shown compared to the averaged natural value to show instrumental precision. Interferences in BHVO-2 and trinitite were observed at ^{140}Ce signal <1 mV and ^{147}Sm<10^{-3} mV. Results for ^{142}Nd are corrected for ^{142}Ce interference. All isotopic ratios are corrected to ^{146}Nd/^{144}Nd = 0.7219. Shaded regions refer to 2σ uncertainty with ^{235}U model uncertainty comparable to ^{239}Pu.

584 **Table 1** The instrumental operation conditions used for LA-ICP-MS analysis

New Wave Nd: YAG laser parameters	
Wavelength	213 nm
Energy density	2-3 J cm^{-2}
Pulse duration	5 ns
Carrier gas	He
Ablation pattern	Single spot
Laser beam size (diameter)	40 μm (NIST 610), 80 μm (Trinitite)
Repetition rate	7 Hz
Thermo Finnigan Element2 ICP-MS parameters	
RF power	1250 W
HV	8 kV
Scan optimization	Speed (dynamic peak-hopping mode)
Mass resolution	300 (m/Δm)
Detection mode	Analog and counting
Sampler cone	1.0 mm Al-alloy
Skimmer cone	0.7 mm Al-alloy
Cool gas flow	16 L min^{-1} Ar
Auxiliary gas flow	1.5 L min^{-1} Ar
Sample gas flow[a]	0.8 L min^{-1} Ar
Carrier gas flow[a]	0.6 L min^{-1} He
Dwell time	5 ms at masses: 43, 137, 139, 140, 141, 142, 143, 144, 145, 146, 147, 148, 149, 150, 151, 152, 153, 154, 155, 156, 157, 158, 159, 160, 161, 162, 163, 164 10ms at masses: 165, 166, 167, 168, 169, 170, 171, 172, 173, 174, 175, 176

585 [a]These gas flows were coupled at a T-junction prior to the plasma torch.

586

Table 2 The instrumental operation conditions used for MC-ICP-MS analysis

Nu Plasma HR MC-ICP-MS parameters[a]	
RF power	1300 W
Reflected power	5 W
Accelerating voltage	4000 V
Cool gas flow	13 L min^{-1} Ar
Auxiliary gas flow	1 L min^{-1} Ar
Sweep gas flow[b]	2.75 L min^{-1} Ar
N_2 gas	10 mL min^{-1} N_2
Aspiration rate	50 μL min^{-1}
Integration time	10s
Blocks	5
Background time	30s between blocks
Nu Plasma HR2 MC-ICP-MS parameters[c]	
RF power	1300 W
Reflected power	0 W
Accelerating voltage	6000 V
Cool gas flow	13 L min^{-1} Ar
Auxiliary gas flow	0.8 L min^{-1} Ar
Sample gas flow[d]	4.5 L min^{-1} Ar
Aspiration rate	100 μL min^{-1}
Integration time	10s
Blocks	5
Background time	30s between blocks

[a] University of Maryland – Nd isotopes
[b] Gas flows were set using an Aridus I
[c] Savannah River National Laboratory – Gd isotopes
[d] Gas flows were set using a DSN-100

593 **Table 3** Major element oxide composition obtained via EPMA analysis of trinitite

	E1[a]	E2	E3	E4	E5	E6	E7	E8	E9
Oxide wt%									
SiO_2	64.74	64.96	65.43	67.72	68.14	65.52	57.10	65.03	96.42
TiO_2	0.08	0.03	0.08	0.54	0.45	0.37	0.92	0.62	b.d.[b]
Al_2O_3	18.81	19.46	18.21	15.25	13.86	17.31	13.25	11.82	0.15
FeO	1.15	0.28	1.05	3.15	2.53	2.71	6.57	2.55	0.16
MnO	0.02	b.d.[b]	0.02	0.07	0.06	0.06	0.09	0.05	b.d.[b]
MgO	0.39	0.03	0.44	1.30	1.06	1.00	2.74	0.94	0.06
CaO	0.38	1.27	4.62	6.66	7.00	7.10	15.15	8.68	0.32
Na_2O	2.14	2.61	2.05	2.09	1.82	2.21	1.71	2.04	0.20
K_2O	10.25	10.32	7.92	3.55	3.32	3.17	2.32	3.05	0.30
Total	97.96	98.96	99.82	100.33	98.24	99.45	99.85	94.78	97.61

594 [a]Locations in Figure 3

595 [b]Below detection.

596

Table 4 Trace element results obtained via LA-ICP-MS with concentrations in µg/g obtained via ablation yield normalization

	L1[a]	L2	L3	L4	L5	L6	L7	L8	L9	L10	L11
La	1.4 ± 0.1	22.8 ± 0.7	25.3 ± 0.6	39.0 ± 0.9	1.3 ± 0.2	16.0 ± 0.5	32.6 ± 0.8	38 ± 1	33.6 ± 0.8	n.m.[c]	n.m.
Ce	2.5 ± 0.2	43 ± 1	48 ± 1	74 ± 1	5.3 ± 0.6	32.7 ± 0.9	65 ± 1	80 ± 2	69 ± 1	n.m.	n.m.
Pr	0.15 ± 0.04	5.4 ± 0.2	5.7 ± 0.2	8.2 ± 0.3	0.4 ± 0.1	3.7 ± 0.2	7.1 ± 0.3	8.6 ± 0.4	8.0 ± 0.3	n.m.	n.m.
Nd	0.57 ± 0.2	20 ± 2	24 ± 2	32 ± 2	1.2 ± 0.4	13 ± 1	27 ± 2	29 ± 2	28 ± 2	n.m.	n.m.
Sm	0.2 ± 0.1	4.0 ± 0.5	4.8 ± 0.5	4.8 ± 0.6	0.3 ± 0.1	2.4 ± 0.4	4.5 ± 0.5	4.8 ± 0.6	5.8 ± 0.6	n.m.	n.m.
Eu	0.7 ± 0.1	0.9 ± 0.1	1.3 ± 0.2	0.7 ± 0.1	0.04 ± 0.03	0.6 ± 0.1	1.2 ± 0.1	1.1 ± 0.2	1.2 ± 0.2	n.m.	n.m.
Gd	0.3 ± 0.2	3.2 ± 0.4	4.5 ± 0.5	3.8 ± 0.5	0.4 ± 0.1	2.3 ± 0.3	3.2 ± 0.4	4.2 ± 0.5	5.0 ± 0.5	n.m.	n.m.
Tb	0.05 ±0.02	0.57 ± 0.06	0.73 ± 0.06	0.42 ± 0.06	0.04 ± 0.02	0.40 ± 0.05	0.62 ± 0.06	0.56 ± 0.07	0.83 ± 0.08	n.m.	n.m.
Dy	0.28 ± 0.09	2.9 ± 0.3	4.8 ± 0.3	2.6 ±0.3	0.3 ± 0.1	3.1 ± 0.3	4.7 ± 0.3	3.9 ± 0.4	5.5 ± 0.4	n.m.	n.m.
Ho	0.06 ± 0.01	0.60 ± 0.05	1.03 ± 0.06	0.49 ± 0.04	0.04 ± 0.01	0.60 ± 0.04	0.95 ± 0.05	0.87 ± 0.06	1.1 ± 0.06	n.m.	n.m.
Er	0.17 ± 0.04	1.9 ± 0.1	3.2 ± 0.2	1.5 ± 0.1	0.16 ± 0.05	2.0 ± 0.1	3.3 ± 0.2	2.7 ± 0.2	3.4 ± 0.2	n.m.	n.m.
Tm	0.04 ± 0.01	0.29 ± 0.03	0.48 ± 0.04	0.20 ± 0.03	0.02 ± 0.01	0.35 ± 0.03	0.57 ± 0.04	0.45 ± 0.04	0.54 ± 0.04	n.m.	n.m.
Yb	0.22 ± 0.06	2.0 ± 0.2	3.3 ± 0.2	1.4 ± 0.1	0.20 ± 0.06	2.2 ± 0.2	4.1 ± 0.2	3.5 ± 0.2	4.0 ± 0.2	n.m.	n.m.
Lu	0.04 ± 0.01	0.39 ± 0.04	0.50 ± 0.04	0.24 ± 0.03	0.02 ± 0.01	0.38 ± 0.04	0.60 ± 0.04	0.48 ± 0.04	0.57 ± 0.04	n.m.	n.m.
^{238}U	n.m.	43.0 ± 0.4	46.5 ± 0.3	n.m.	n.m.	n.m.	n.m.	41.8 ± 0.4	276 ± 2	29.1 ± 0.2	27.8 ± 0.3
^{239}Pu[b]	n.m.	0.36 ± 0.04	2.22 ± 0.07	n.m.	n.m.	n.m.	n.m.	1.70 ± 0.07	0.56 ± 0.1	0.56 ± 0.03	0.59 ± 0.04
^{240}Pu[b]	n.m.	0.012 ± 0.006	0.036 ± 0.009	n.m.	n.m.	n.m.	n.m.	0.06 ± 0.01	0.02 ± 0.02	0.018 ± 0.006	0.009 ± 0.005
^{240}Pu/^{239}Pu	n.m.	0.034 ± 0.018	0.016 ± 0.004	n.m.	n.m.	n.m.	n.m.	0.033 ± 0.008	0.027 ± 0.028	0.033 ± 0.011	0.015 ± 0.008

[a]Locations Figure 3

[b]Pu concentration calculated based on assumed similar ablation and ionization yields as ^{238}U

[c]Not measured: No data collected for these elements

Table 5 Nd and Gd isotopic ratios for standards and trinitite sample

Sample		$^{142}Nd/^{144}Nd$	$^{143}Nd/^{144}Nd$	$^{145}Nd/^{144}Nd$	$^{148}Nd/^{144}Nd$	$^{150}Nd/^{144}Nd$	^{140}Ce (V)	^{147}Sm (V)
Nd-Ames Metal (n=18)[a]		1.141863	0.512151	0.348403	0.241543	0.236353	-	-
	2σ	0.000053	0.000018	0.000012	0.000010	0.000009	n/a	n/a
BHVO-2 (n=2)[a]		1.141884	0.512995	0.348389	0.241542	0.236346	0.0013	0.000009
	2σ	0.000041	0.000033	0.000003	0.000003	0.000002	0.0002	0.000005
Trinitite (n=1)[a]		1.141751	0.512164	0.348474	0.241567	0.236342	0.0012	0.000005
	2σ	0.000025	0.000009	0.000005	0.000007	0.000010	0.0002	0.000014

Sample		$^{155}Gd/^{160}Gd$	$^{156}Gd/^{160}Gd$	$^{157}Gd/^{160}Gd$	$^{158}Gd/^{160}Gd$	^{147}Sm (V)	^{162}Dy (V)
Gd Solution (n=20)		0.676819	0.9361	0.715875	1.135906	-	-
	2σ	0.000042	n/a	0.000033	0.000040	n/a	n/a
BHVO-2 (n=2)[b]		0.676813	0.9361	0.715884	1.135883	0.00006	0.00022
	2σ	0.000017	n/a	0.000012	0.000028	0.00001	0.00001
Trinitite (n=1)[b]		0.677097	0.936492	0.715880	1.136301	0.00004	0.00210
	2σ	0.000064	0.000070	0.000042	0.000044	0.00002	0.00020

[a] $^{142}Nd/^{144}Nd$ normalized to $^{146}Nd/^{144}Nd = 0.7219$

[b] $^{155}Gd/^{160}Gd$ normalized to $^{156}Gd/^{160}Gd = 0.9361$ using standard-sample bracketing

606 **Table 6** List of independent and cumulative yield of lanthanoids of interest [8]
607

	Independent Yield (%)	Cumulative Yield (%)	Initial Isotope	Lifetime (minutes)
^{142}Nd	2±1 x10^{-10}	1.2±0.7 x10^{-6}	^{142}Pr	2x10^{3}
^{144}Nd	2.8±0.9 x10^{-9}	3.69±0.03	^{144}Ba	6x10^{5}
^{145}Nd	4±2 x10^{-6}	3.00±0.02	^{145}La	3x10^{1}
^{146}Nd	8±5 x10^{-5}	2.46±0.01	^{146}Ce	3x10^{1}
^{148}Nd	7±4 x10^{-3}	1.658±0.006	^{148}Ce	3x10^{0}
^{150}Nd	1.0±0.6 x10^{-1}	0.993±0.005	^{150}Pr	1x10^{-1}
^{155}Gd	3±2 x10^{-7}	0.21±0.02	^{155}Pm	4x10^{6}
^{156}Gd	7±2 x10^{-7}	0.154±0.006	^{156}Pm	3x10^{4}
^{157}Gd	3±2 x10^{-5}	0.106±0.008	^{157}Sm	1x10^{3}
^{158}Gd	2±1 x10^{-4}	0.06±0.01	^{158}Sm	5x10^{2}
^{160}Gd	1.1±0.7 x10^{-3}	0.016±0.005	^{160}Eu	9x10^{-1}

608

609
610